Chapter 13
NIR Fluorescent Nanoprobes and Techniques for Brain Imaging

Takashi Jin and Yasutomo Nomura

13.1 Introduction

For in vivo fluorescence imaging, visible-emitting fluorescent probes cannot be applied because of the strong absorption and scattering of visible light by intrinsic chromophores, organelles, and cytoskeleton in cells [1, 2]. Most of the visible-emitting fluorescent probes have been used for in vitro imaging and sensing of biomolecules and organelles using conventional fluorescence microscopes [3, 4]. Compared with visible light (400–700 nm), NIR light (700–1400 nm) allows deeper penetration with reduced absorption and scattering in living tissues [5]. In addition, tissue autofluorescence in the NIR region is much lower than the autofluorescence in the visible region [5]. Thus, NIR fluorescence imaging is widely used for non-invasive visualization of deep tissues in living system [6–9].

So far, conventional NIR region ranging from 700 to 900 nm (1st NIR window) has been used for in vivo imaging [5]. In this NIR region, many kinds of fluorescent probes such as Cy7, ICG, iRFP, and CdSeTe quantum dots (QDs) are commercially available (Fig. 13.1). Recently, NIR fluorescence imaging in the wavelengths of 1000–1400 nm (2nd NIR window) [10–14] has been attracted for clearer deep-tissue imaging at the whole-body level (Fig. 13.2). As the tissue autofluorescence and scattering significantly decrease beyond 1000 nm, 2nd NIR fluorescence

T. Jin (✉)
Laboratory for Nano-Bio Probes, RIKEN Center for Biosystems Dynamics Research, Suita, Japan

Graduate School of Frontier Biosciences, Osaka University, Ibaraki, Japan
e-mail: tjin@riken.jp

Y. Nomura
Laboratory for Nano-Bio Probes, RIKEN Center for Biosystems Dynamics Research, Suita, Japan

Department of Systems Life Engineering, Maebashi Institute of Technology, Maebashi, Japan
e-mail: ynomura@maebashi-it.ac.jp

A. Benayas et al. (eds.), *Near Infrared-Emitting Nanoparticles for Biomedical Applications*, https://doi.org/10.1007/978-3-030-32036-2_13

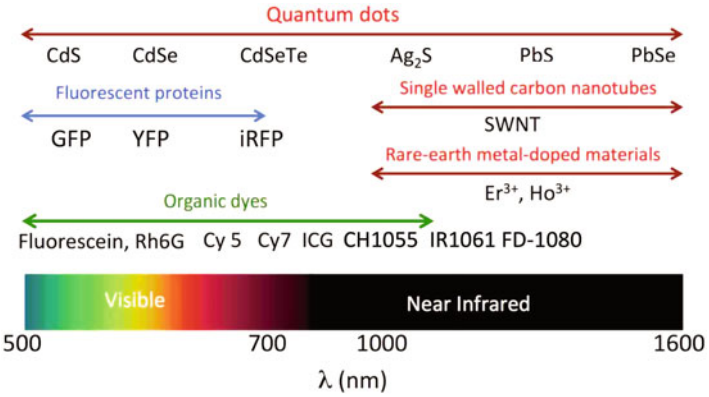

Fig. 13.1 Representative nanoprobes that can be used for bioimaging at the wavelengths of visible and near infrared regions

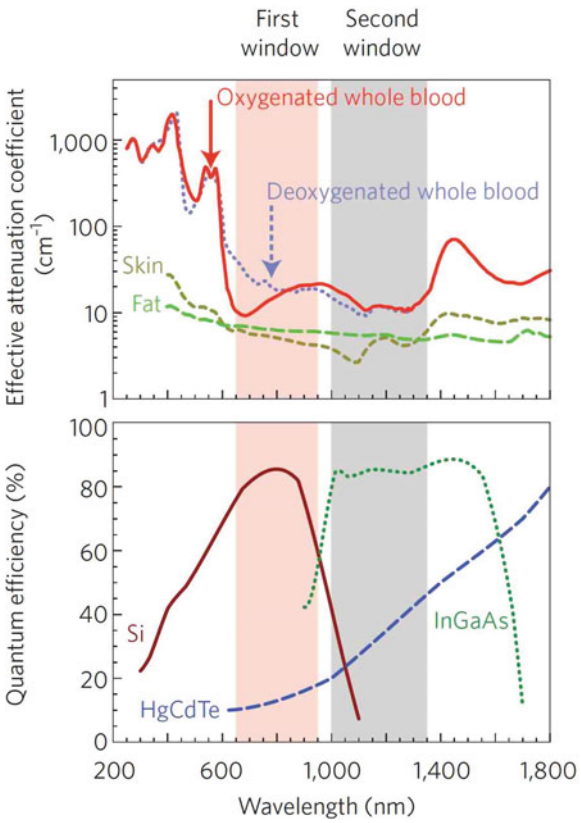

Fig. 13.2 First and second NIR windows in biological tissues. Top: These plots of effective attenuation coefficient (on a log scale) versus wavelength show that absorption and scattering from oxygenated blood, deoxygenated blood, skin, and fatty tissue is lowest in either the first (pink shaded area) or 2nd (grey) NIR window. Bottom: Sensitivity curves for typical cameras based on silicon (Si), indium gallium arsenide (InGaAs) or mercury cadmium telluride (HgCdTe) sensors. Reproduced from ref. [10] with permission from Springer-Nature

imaging offers better spatiotemporal resolution in the deep-tissue imaging [10–12]. Unfortunately, compared with conventional NIR fluorescent probes in the 1st NIR window, NIR fluorescent probes that can be used in the 2nd NIR window are very limited.

During the past 5 years, several types of NIR fluorescent probes such as single-walled carbon nanotubes (SWNTs) [15–32], PbS QDs [33–43], Ag_2S QDs [44–57], and rare earth-doped nanoparticles [58–61] have been developed for in vivo imaging in the 2nd NIR window. Recently, organic dye-based NIR nanoprobes with low toxicities have attracted much attention for deep-tissue imaging in the 2nd NIR window [62–91]. In this chapter, we focus on the synthesis, optical properties, and applications of NIR fluorescent nanoprobes for non-invasive brain imaging in the 2nd NIR window.

13.2 Optical Property of Brain Tissue

In non-invasive fluorescence imaging of brain, autofluorescence, absorption, and scattering by scalp and skull significantly affect the signal-to-background ratios of the fluorescence images. Autofluorescence and absorption result mainly from the intrinsic chromophores such as nicotinamide adenine dinucleotide phosphate (NADP) and flavin in intracellular compartments [92–94]. To get clear NIR fluorescence images of mouse brains, excitation wavelengths are very important to reduce the absorption and autofluorescence by tissues. The detection wavelengths for fluorescence emission are also important to get reduced scattering images.

The absorption spectrum of a mouse brain shows that tissue absorption at the NIR region from 700 to 1400 nm is very low (Fig. 13.3a). The strong absorption at

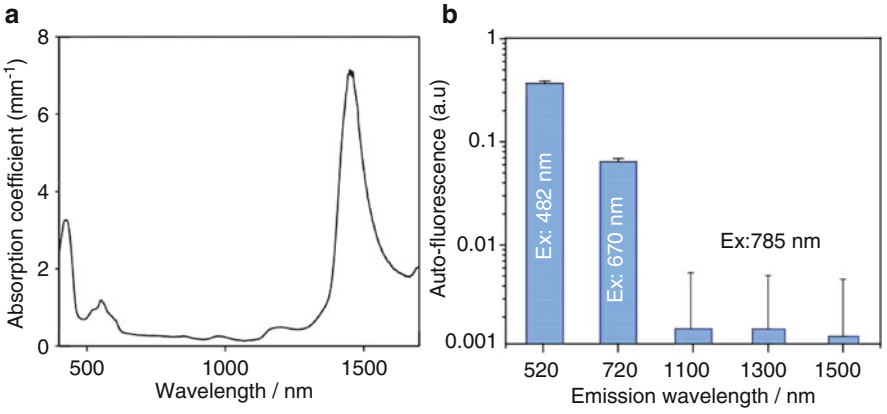

Fig. 13.3 (**a**) Absorption spectrum of a mouse brain. (**b**) Autofluorescence of a mouse brain. The fluorescence at 520 and 720 nm was obtained by excitation at 482 and 670 nm, respectively. The fluorescence at 1110, 1300, and 1500 nm was obtained by excitation at 785 nm. Adapted from ref. [41]

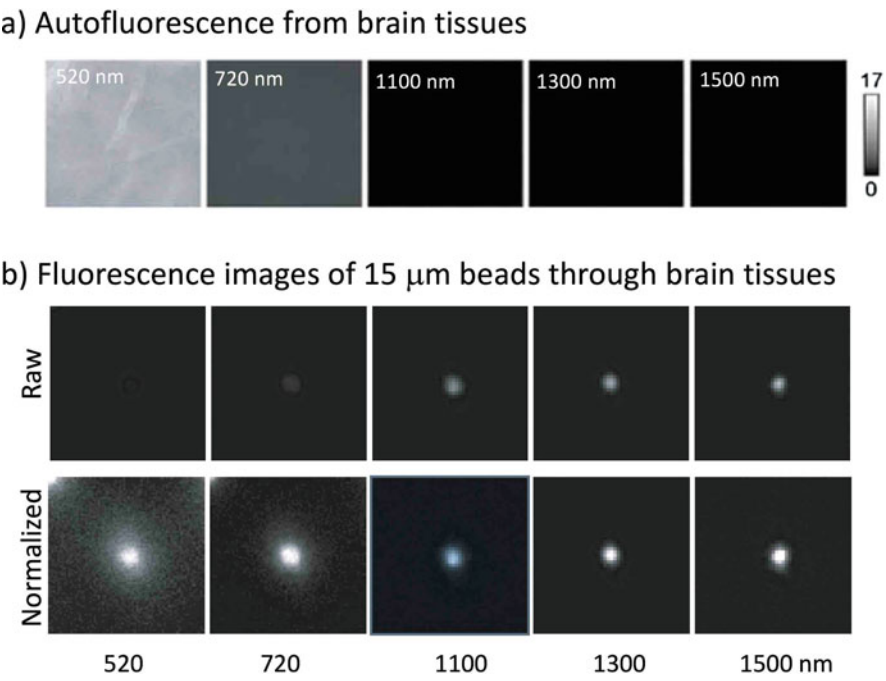

Fig. 13.4 (**a**) Autofluorescence from brain tissues of mice. The autofluorescence at 520 and 720 nm was measured by excitation at 482 and 670 nm, respectively. The autofluorescence over 1000 nm was measured by excitation at 785 nm. (**b**) Fluorescence images of 15 μm beads containing five types of QDs (520, 720, 1100, 1300, and 1500 nm emission) though brain tissues of mice. Thickness of the brain tissues was 100 μm. The intensity of fluorescence emission of each QDs was adjusted to the similar level. Upper images show raw data, and lower images show normalized data. Reproduced from ref. [36] with permission from Royal Society of Chemistry

the visible region less than 600 nm is attributed to the absorption by intrinsic chromophores such as flavin and hemoglobin. The intense absorption at around 1500 nm is due to the absorption by water molecules in the brain tissue. Autofluorescence of the mouse brain strongly depends on the wavelength of excitation (Fig. 13.3b). The intensity of autofluorescence over 1000 nm is very low compared with that of the autofluorescence at 520 and 720 nm. Figure 13.4a shows autofluorescence images (at 520, 720, 1100, 1300, and 1500 nm) of brain tissues. It should be noted that the autofluorescence intensity decreases with increasing the emission wavelength, indicating intrinsic chromophores in tissues are less excited at longer wavelengths. Furthermore, the tissue scattering of NIR fluorescence decreases with increasing the emission wavelength (Fig. 13.4b). These optical properties in the 2nd NIR window allow clearer deep-tissue imaging of brain with high signal-to-background ratios, compared with the imaging performed at the visible and 1st NIR regions.

13.3 NIR Nanoprobes for In Vivo Fluorescence Imaging

13.3.1 Nanomaterial-Based NIR Nanoprobes

SWNTs in the 2nd NIR window the first-reported fluorescent nanoprobes by Dai group for intravital imaging in mice [24]. SWNTs are cylindrical nanotubes (hundred nanometer in length) consisting of graphene layers, and they have a broad emission in the 2nd NIR region [15]. Although raw SWNTs are insoluble to water and their fluorescence quantum yields are very low (<1%), surface functionalization results in water-dispersible and bright SWNTs [24]. So far, several groups have demonstrated the capability of surface-functionalized SWNTs as NIR fluorescent probes for non-invasive imaging of organs, lymph nodes, tumors, and cerebral vessels in mice [25–32]. For biomedical applications, SWNTs have serious problems on their cytotoxicity and difficulty in exclusion from the body [15, 95, 96].

Nanoparticle-based NIR nanoprobes such as Ag_2S QDs, PbS QDs, rare earth-doped nanoparticles are alternative NIR nanoprobes for intravital imaging in the 2nd NIR window (Fig. 13.5). NIR-emitting Ag_2S QDs [44–57], and PbS QDs [33–43]

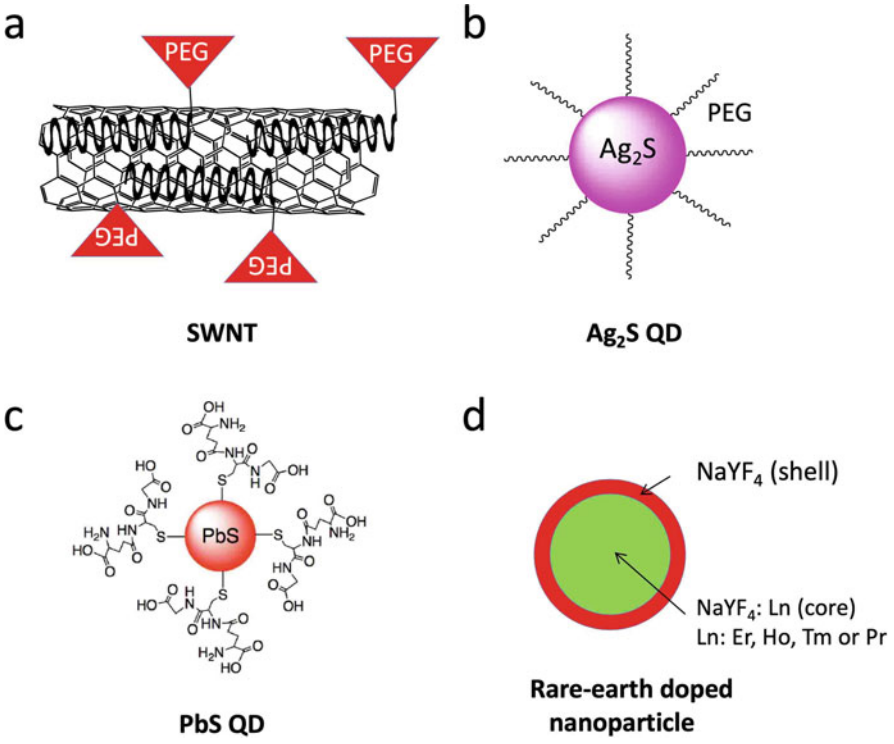

Fig. 13.5 Schematic illustration of typical nanomaterial-based NIR nanoprobes, (**a**) Polyethylene glycol (PEG)-capped SWNT [24], (**b**) PEG-capped Ag_2S QDs [45], (**c**) glutathione-capped PbS QDs [33], and (**d**) rare earth-doped nanoparticle [59]

are semiconductor nanocrystals that have unique optical properties, such as size-dependent tunable emissions, narrow emission bands, high quantum yields, and high resistance to photobleaching. In 2010, Wang group first synthesized NIR-emitting Ag_2S QDs for bioimaging by thermal decomposition of $(C_2H_5)_2NCS_2Ag$ [44]. By optimization of the reaction conditions for preparing QDs, they succeeded in the synthesis of emission tunable Ag_2S QDs with a high quantum yield (ca. 20%) in the wavelength region from 900 to 1200 nm [52]. Furthermore, they demonstrated the capability of the Ag_2S QDs for tumor imaging, in situ tracking of transplanted stem cells, and imaging-guided precise operation of glioma [46, 54–56]. In 2013, our group reported a facile method for preparing water-dispersible PbS QDs, which have tunable emissions from 1000–1400 nm with high quantum yields of 6–12% [33]. As the water-dispersible PbS QDs are capped with glutathione (a natural tripeptide), functionalized QDs with biomolecules such as antibody and peptide are easily prepared. We demonstrated the utility of the PbS QDs for non-invasive visualization of lymph nodes as well as breast tumors in living mice. Furthermore, we synthesized highly bright PbS/CdS QDs with a core/shell structure that emit from 1000 to 1500 nm, and we applied these QDs to non-invasive imaging of cerebral blood vessels in mice [34]. In this work, we found that the signal-to-background ratio in the NIR fluorescence imaging of brain tissue at 1300 nm can be improved 76 times compared to the NIR imaging at 720 nm. In 2013, Moghe group reported rare earth (Er^{3+}, Ho^{3+}, Tm^{3+}, and Pr^{3+})-doped nanoparticles as in vivo shortwave infrared reports for intravital imaging in mice [59]. Other groups also reported rare-earth nanoparticles for organ imaging and cancer early detection [58, 60, 61]. However, biomedical applications of these nanoparticle-based NIR nanoprobes including SWNTs are very limited due to their dose-dependent toxicity [95, 96].

13.3.2 Organic Dye-Based NIR Nanoprobes

Recently, organic dye-based NIR nanoprobes emitting over 1000 nm have been developed as next-generation NIR nanoprobes for intravital bioimaging. Although a variety of NIR organic nanoprobes emitting in the 1st NIR window are commercially available, there are a very limited number of NIR organic nanoprobes that emit over 1000 nm. During a few years, several types of NIR-emitting organic dyes beyond 1000 nm have been reported for bioimaging. Organic dye-based NIR nanoprobes are classified into three types (Fig. 13.6a). Frist type is NIR-dye nanoparticles, where NIR dyes are incorporated into micelles or amphiphilic polymers [62, 63]. Second type is NIR-dye complex, where NIR dyes are conjugated to proteins such as fetal bovine serum [64]. Third type is solely, water-dispersible NIR dyes [65, 67]. To date, these types of organic dye-based NIR nanoprobes have appeared as probes for bioimaging in the 2nd NIR window (Fig. 13.6b). Compared with nanomaterial-based NIR nanoprobes, organic dye-based nanoprobes have well-defined architectures with rapid metabolism and low toxicity [66, 97].

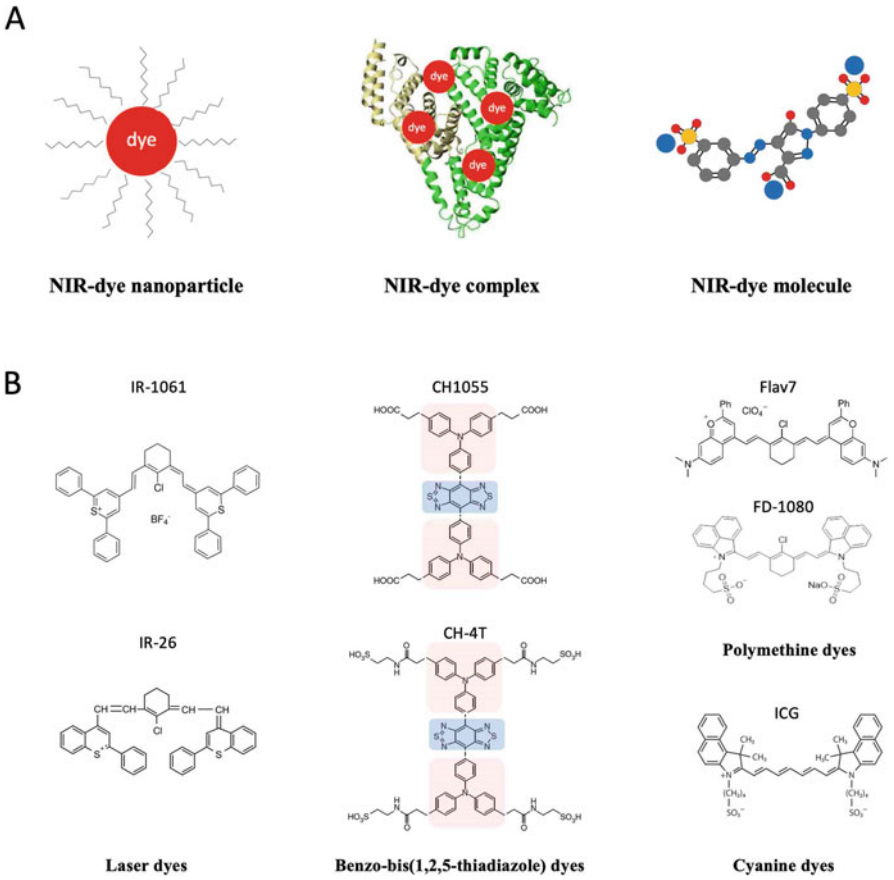

Fig. 13.6 (**a**) Schematic illustration of three types of organic dye-based NIR fluorophore. (**b**) Chemical structures of typical NIR dyes emitting over 1000 nm (laser dyes, benzo-bis (1,2,5-thiadiazole) dyes, polymethine dyes, and cyanine dyes). Blue and pink color show the electron acceptor and donor unit, respectively

In 2013, Dai group reported laser dye, IR-1061 incorporated nanoparticles as a NIR nanoprobe for in vivo imaging [62]. IR-1061 is a commercially available polymethine dye, which is highly hydrophobic and insoluble to water. Thus, they incorporated IR-1061 to nanoparticles consisting of amphiphilic polymer poly (acrylic acid, PAA) and polyethylene glycol-conjugated phospholipid (DSPE-nPEG). The fluorescence quantum yield of the IR-1061 incorporated nanoparticle was 1.8% [62]. They succeeded in performing whole-body imaging of nude mice after intravenous injection of the IR-1061 incorporated nanoparticles. They found the facile excretion of the IR-1061 nanoparticles from the body. Using the similar strategy, Dai group also reported fluorescent copolymer (poly(benzo[1,2-b:3,4-b']difuran-*alt*-fluorothieno-[3,4-b]thiophen, pDA) incorporated nanoparticles as a

NIR nanoprobe and performed ultrafast fluorescence imaging (>25 flames/sec) in the 2nd NIR window [63].

In the design of NIR-emitting nanoprobes, the energy band gap is known to be significantly affected by conjugation length as well as donor–acceptor (D–A) charge transfer in π-conjugated molecules [78]. In 2016, Dai, Cheng and Hong reported a new type of benzo-bis(1,2,5-thiadiazole) NIR-emitting dyes with D–A–D charge structures (Fig. 13.6b) [65, 69, 80]. This type of NIR nanoprobe (CH1055-PEG) emits at approximately 1050 nm with a quantum yield of 0.3% in an aqueous solution [65]. They modified the fluorescence brightness of CH1055 by complexation of its sulfonated derivative (CH-4T) with bovine serum to produce 110-fold increase in NIR fluorescence. They succeeded to perform molecular imaging of tumors in mice using affibody-functionalized CH1055 [65], leading to a possible application of the NIR dye to tumor detection in humans. Their works showed that the brightness of D–A–D dyes can be significantly improved by their composites with proteins. To date, several derivatives of benzo-bis(1,2,5-thiadiazole) nanoprobes have been reported for in vivo tumor imaging and image-guided surgery [68, 78].

In 2017, Sletten group reported flavylium polymethine nanoprobes for near- and shortwave-infrared imaging [79]. They synthesized a new series of polymethine dyes with dimethylamino flavylium heterocycles and found that a flavylium dye (Flav 7) emitting at ca. 1050 nm is 13 times brighter than IR-26 (quantum yield: 0.05). They achieved whole-body imaging of nude mice by intravenous injection of Flav 7 micelles consisting of mPEG-DSPE lipids, suggesting the possible translation of polymethine nanoprobes to optical diagnostics in NIR region over 1000 nm. In 2018, Zhang group reported the synthesis and application of a cyanine dye (FD-1080) that emit at around 1100 nm for deep-tissue high-resolution dynamic bioimaging [67]. The excitation wavelength (1064 nm) of this NIR probe was longer than that (650–980 nm) of previous reported NIR probe. Thus, this NIR probe allowed deeper tissue imaging due to the high penetration of excitation light (1064 nm). The quantum yield of PD-1080 was 0.31% in an aqueous solution and could be increased to 5.94% after combining with fetal bovine serum. This dye is the first-reported NIR nanoprobe that can be excited at the wavelength longer than 1000 nm.

More recently, several groups have found that a commercially available dye, indocyanine green (ICG) with an emission peak of 830 nm can be used to NIR fluorescence imaging in the 2nd NIR window [72, 73, 83, 85]. ICG is the only NIR nanoprobe that is approved by the Food and Drug Administration (FDA) for clinical use in humans. Although the NIR emission of ICG over 1000 nm is very week, its emissions in blood and vasculatures are clearly detected by an InGaAs camera. In 2018, Bawendi and Bruns group showed that ICG can be used as a NIR nanoprobe for in vivo fluorescence imaging over 1000 nm, including intravital microscopy, non-invasive real-time imaging in blood and lymph vessels, imaging of hepatobiliary clearance, and molecular targeted in vivo imaging [73]. In the same year, Annapragada group reported that ICG-incorporated liposomes show higher contrast to noise ratios compared to free ICG in the 2nd NIR window, allowing visualization of hind limb and intracranial vasculatures [72, 83]. Sun and Chen

group reported that the NIR emissions of ICG including IRDye800 and IR-12N3 have the potential to accelerate clinical translation of NIR fluorescence imaging in the 2nd NIR window [85]. While no FDA-approved NIR organic nanoprobes with an emission peak over 1000 nm exist, the emission of ICG may give rapid translation of longer NIR fluorescence to humans in clinical applications.

13.4 NIR Fluorescence Detection System for Brain Imaging

In most of the commercially available in vivo imaging systems, conventional NIR wavelenths ranging from 700 to 900 nm (1st NIR optical window) are used for deep-tissue imaging. This is because the conventional NIR photodetectors (silicon CCD camera) are sensitive in the 1st NIR region, and 1st NIR-emitting probes (e.g., Indocyanine green, Cy 7, and CdSeTe QDs) are commercially available. Although 1st NIR fluorescence imaging is useful for the non-invasive visualization of organs and tissues, its spatial resolution is not enough to observe cellular dynamics. As tissue autofluorescence and scattering significantly decrease with increasing the excitation/emission wavelength, fluorescence imaging in the 2nd NIR region should be very useful to get better spatiotemporal resolution in deep-tissue imaging [10]. However, there are no commercially available imaging systems with high spatiotemporal resolution in the 2nd NIR window.

Our 2nd NIR microscope imaging system is based on the Macro Zoom System with zoom function from 0.63× to 6.3× (Fig. 13.7). Optical system is optimized for VIS, 1st NIR, and 2nd NIR fluorescence imaging. Solid-state lasers for 645, 785, and 978 nm excitation, and emission filters of 1100 ± 25 nm, 1300 ± 25 nm, and 1500 ± 25 nm are equipped to the optical system. A Xe lamp was used as the excitation light source at 482 nm for VIS imaging. A Si EM camera (iXon3, Andor) is used for VIS and 1st NIR fluorescence imaging, and an InGaAs CMOS camera (C10633-34; Hamamatsu photonics) is used for 2nd NIR fluorescence imaging.

Dai group used a high-resolution microscopic system for NIR imaging of brain imaging cerebral vessels (Fig. 13.8) [31]. High-magnification intravital imaging of cerebral vessels was carried out in epifluorescence mode with an 808-nm diode laser (RMPC lasers, 160 mW) as the excitation source and two objective lenses (4× and 10×) for microscopic imaging. The mouse with scalp hair removed was intravenously injected with a solution of SWNTs and placed in a home-made stereotactic platform fixed on a motorized 3D-translational stage that allowed for the digital position adjustment and readout of the mouse relative to the objective. The emitted fluorescence was filtered through a 1000-nm long-pass filter, a 1300-nm long-pass filter, and a 1400-nm short-pass filter to ensure only photons in the 1300–1400 nm.

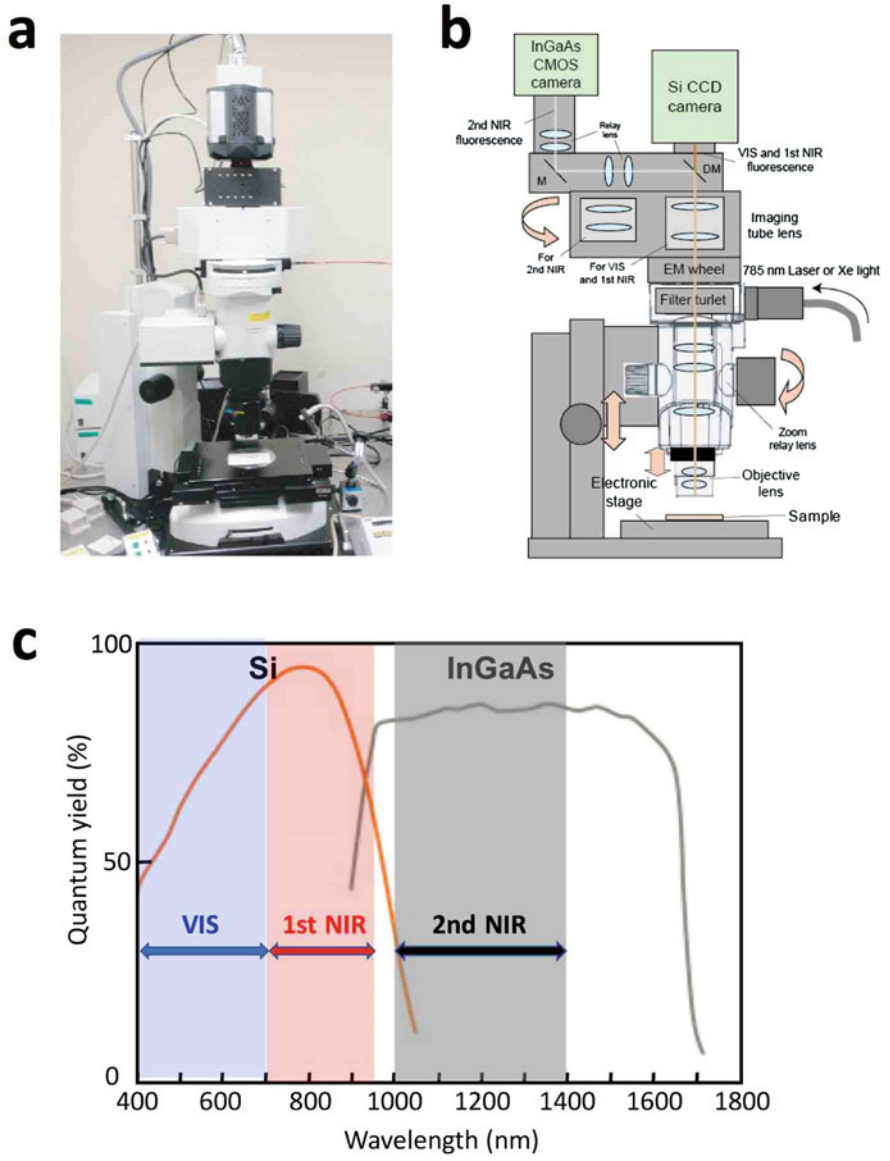

Fig. 13.7 (**a**, **b**) Up-right fluorescence microscope system for in vivo imaging in VIS, 1st NIR, and 2nd NIR region (400–1400 nm). (**c**) Sensitivity curves for typical cameras based on silicon (Si), indium gallium arsenide (InGaAs) sensors. Si and InGaAs cameras are sensitive within the 1st and 2nd NIR windows, respectively

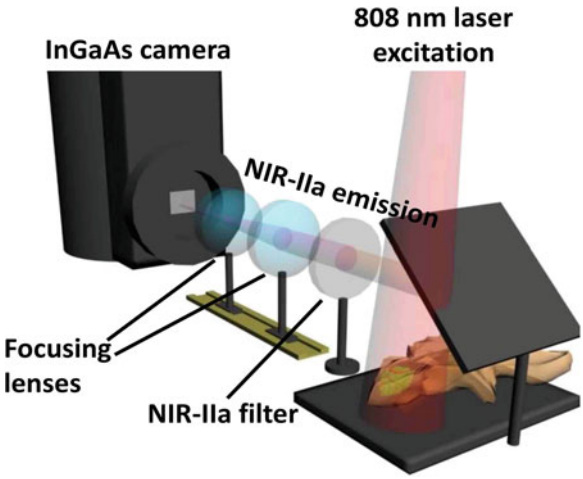

Fig. 13.8 A schematic of NIR fluorescence imaging for non-invasive through-scalp and through-skull brain vascular imaging. NIR-IIa emission: 1300–1400 nm. Reproduce from ref. [31] with permission from Springer-Nature

13.5 Non-invasive Brain Imaging Using NIR Nanoprobes

13.5.1 Cerebral Blood Vessels

13.5.1.1 SWNT Probes

To date, mouse brain imaging has largely relied on magnetic resonance (MR), X-ray computed tomography (CT), and positron emission tomography (PET). However, these imaging modalities have limited spatial resolution and long scanning times. During the past 5 years, a number of reports on non-invasive brain imaging of mice in the 2nd NIR window have appeared using NIR nanoprobes such as SWNTs [31, 98], QDs [34, 41, 99–102], rare earth-doped nanomaterials [104, 105], and organic dyes [65–77, 104–107]. In 2014, Dai et al. first reported 2nd NIR fluorescence imaging of a mouse brain by using (SWNTs) (Fig. 13.9) [31]. They performed through-scalp and through-skull fluorescence imaging of mouse cerebral vasculatures without craniotomy, utilizing the intrinsic photoluminescence of SWNTs in the 1.3–1.4 nm NIR window. They found that reduced photon scattering in the NIR region allowed fluorescence imaging to a depth of >2 mm in mouse brain with sub-10 μm resolution. In this fluorescence imaging, they achieved dynamic NIR fluorescence imaging (5.3 frames/sec) of cerebral blood perfusion.

13.5.1.2 QD Probes

In 2014, our group first reported the non-invasive fluorescence angiography of a mouse head using PbS/CdS QDs in the 2nd NIR window [34]. To date, several types of QDs including PbS QDs, Ag_2S QDs, and InAs QDs have been used for brain imaging in the 2nd NIR window [100–103]. Figure 13.10 shows the fluorescence

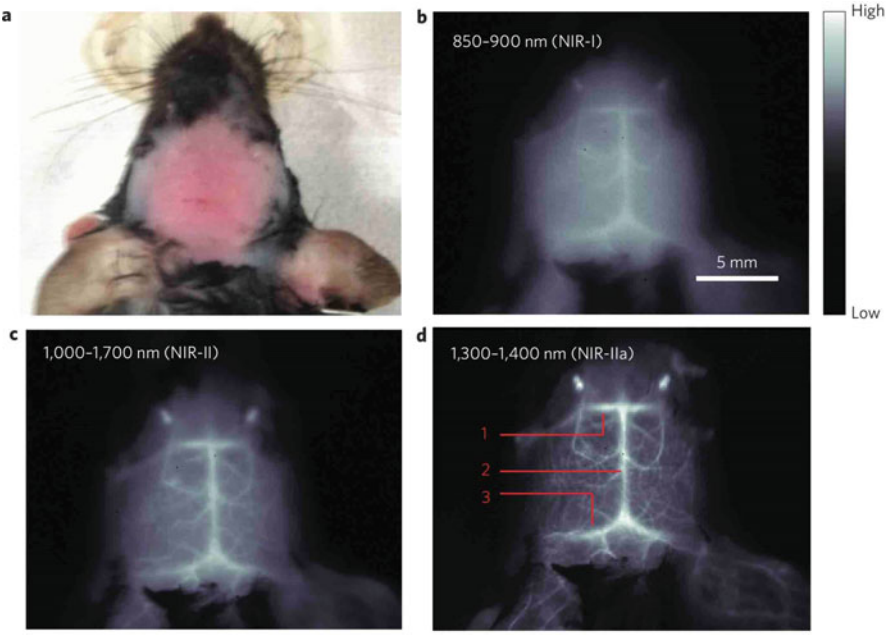

Fig. 13.9 NIR fluorescence imaging of mouse brain vasculatures with SWNT–IRDye800 in different NIR subregions. (**a**), A C57Bl/6 mouse head with the hair removed. (**b–d**), Fluorescence images of the same mouse head in the NIR-I, NIR-II, and NIR-IIa regions. In (**d**), the inferior cerebral vein, superior sagittal sinus, and transverse sinus are labeled 1, 2, and 3, respectively. Reproduced from ref. [31] with permission from Springer-Nature

angiography for a mouse head using bovine serum albumin (BSA)-conjugated VIS, 1st NIR, and 2nd NIR-emitting QDs [34]. The fluorescence images of mouse cerebral vessels were measured by using band-path filters (525, 720, and 1300 nm) after injection of each QDs in a mouse tail vein. Autofluorescence of the mouse body dramatically decreased in the angiography of 2nd NIR images compared with that of the VIS and 1st NIR images. Blood vessels showed a clearer image in the 2nd NIR region due to the higher penetration and lower scattering of the 2nd NIR light in the tissue. The spatial resolution of the fluorescence image of the blood vessels was significantly improved by increasing the imaging wavelength, which also increased the signal-to-background ratio of the 2nd NIR fluorescence images compared with VIS or 1st NIR fluorescence images.

The 2nd NIR fluorescence imaging shows deeper penetration with lower scattering compared with the VIS and 1st NIR fluorescence imaging. Although NIR light over 1000 nm can penetrate across the skin and scalp of the mouse brain, it is difficult to determine the precise value of brain imaging depth in living mice. Figure 13.11 shows the imaging depth for an isolated mouse brain. Visualization depth for the cerebral blood vessels was evaluated by measuring z-stacked images for the isolated brain. In our NIR imaging system, maximum depth for the visualization

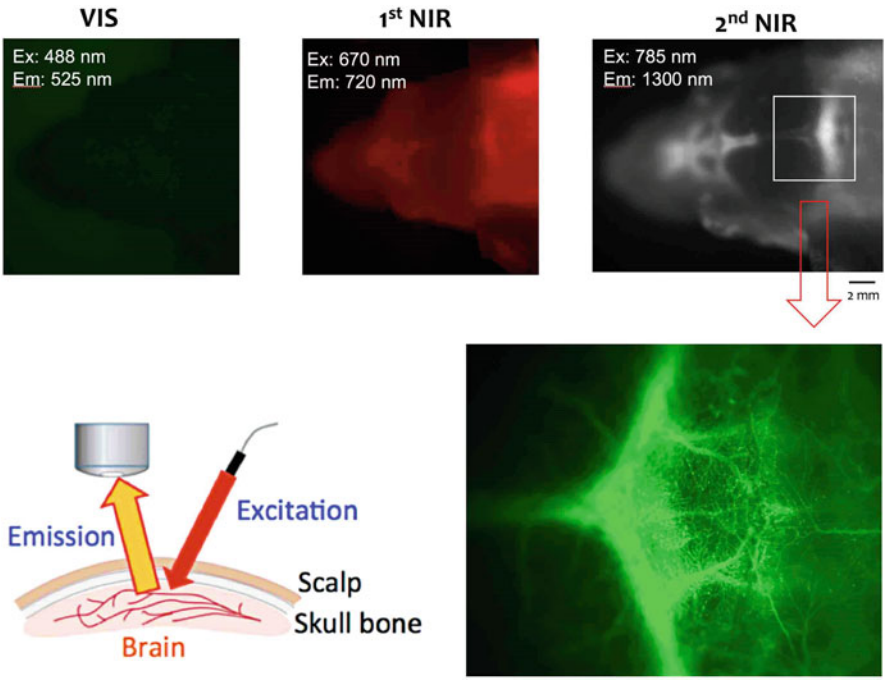

Fig. 13.10 Fluorescence angiography of a mouse head. The images show its Vis (520 nm), 1st NIR (720 nm), and 2nd NIR (1300 nm) fluorescence angiographies, where excitation wavelengths are 488 nm, 670 nm, and 785 nm, respectively. CdSe/ZnS QDs, CdSeTe/CdS QDs, PbS/CdS QDs were used for fluorescence imaging at 525, 720, and 1300 nm, respectively. Reproduced from ref. [34]. Copyright (2014) with permission of Royal Society of Chemistry

of the fine structure of cerebral blood vessels was determined to be ca. 1.6 mm. For a brain of living mouse, we can perform NIR fluorescence imaging of cerebral blood vessels with high spatial resolution. Figure 13.12 shows non-invasive NIR fluorescence images of cerebral blood vessels of a nude mouse after injection of PbS QDs via a tail vein. Immediately after injection of the QDs, strong NIR fluorescence signals were detected and clear images of the cerebral blood vessels could be taken. Although the intensity of the NIR fluorescence signals was gradually decreased, the NIR fluorescence images of the cerebral blood vessels could be taken for ca. 5 minutes post-injection of the PbS QDs. In this brain imaging, we could observe small blood capillaries with a spatial resolution of ca. 10 μm.

13.5.1.3 Rare-Earth Nanoprobes

Rare earth (Er^{3+})-doped nanoprobes can also be used for brain imaging in the NIR window beyond 1500 nm [104, 105]. In general, with increasing the emission wavelength in fluorescence imaging, tissue scattering of the emission light is

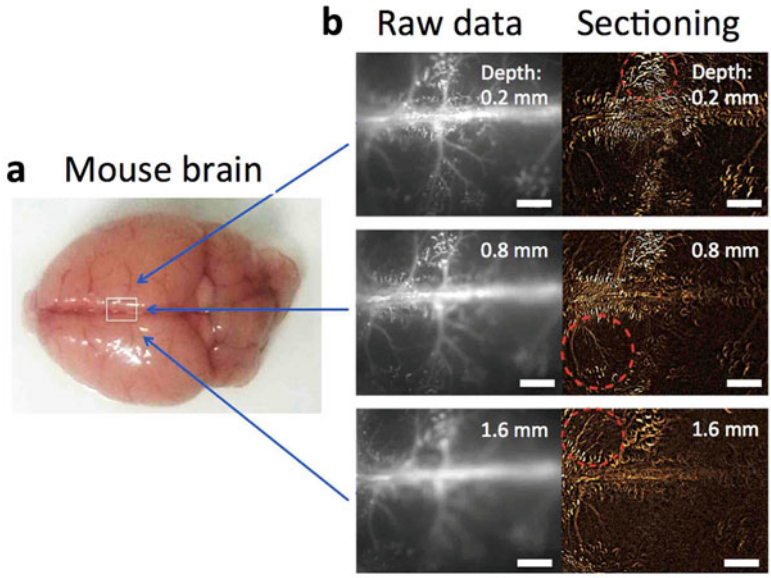

Fig. 13.11 (**a**) Bright-field image of a mouse brain perfused by PbS QDs. (**b**) Raw fluorescence images and sectioning images at the depth of 0.2 mm, 0.8 mm, and 1.6 mm from the surface. The sectioning image was obtained from a raw image minus its previous and next image. Red circles with dotted lines show cerebral blood vessels appearance after sectioning. Scale bar: 1 mm. Adapted from ref. [41]

decreased. Thus, fluorescence imaging beyond 1500 nm would give clearer images of the brain compared with the imaging wavelength in the 2nd NIR region. Zhong et al. reported Er/Ce co-doped $NaYbF_4$ nanocrystals for in vivo fluorescence imaging in the NIR region between 1500 and 1700 nm [104]. This Er/Ce co-doped nanoprobe shows bright emission at 1550 nm under 980 nm excitation. In this probe, Ce doping suppresses the upconversion pathway while boosting down conversion by ninefold to produce bright 1550 nm emission. The authors reported that the quantum yield of this rare-earth nanoprobe was 0.27–2.73% with a highest value among reported down conversion rare earth-doped nanomaterials, leading to fast in vivo cerebrovascular imaging with a 20 ms exposure time in the NIR region between 1500 and 1700 nm (Fig. 13.13).

13.5.1.4 Organic Dye Nanoprobes

Very recently, much attention has been paid to organic dye-based NIR nanoprobes for in vivo imaging in the 2nd NIR window due to their low toxicities and rapid clearance from the body [62–77, 106, 107]. The safety of NIR fluorescent probes is crucial for the application of 2nd NIR fluorescence imaging to biomedical and clinical fields. The fluorescence brightness of organic dye-based NIR nanoprobes

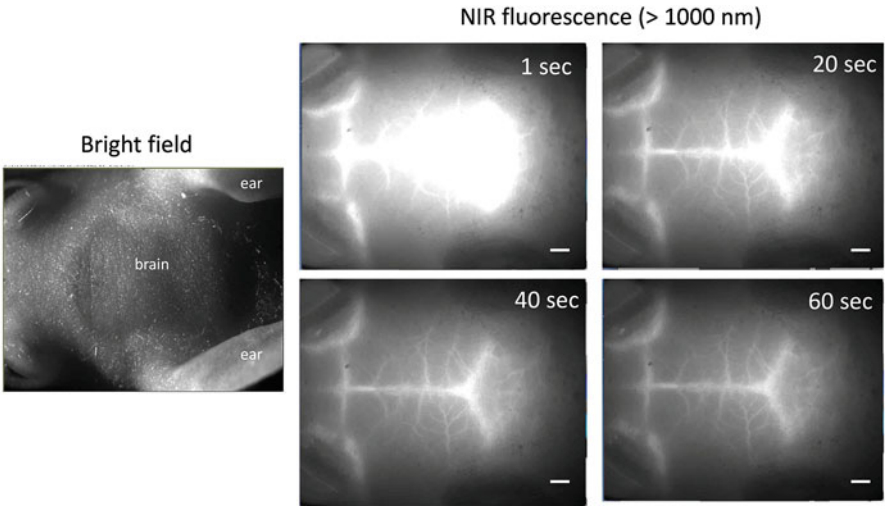

Fig. 13.12 NIR fluorescence images of cerebral blood vessels in a nude mouse. NIR fluorescence images were taken 1 s, 20 s, 40 s, and 60 s post-injection of PbS QDs (200 μL, 2 μM) through a tail vein. Excitation: 670 nm, Emission >1000 nm. Laser power; 25 mW/cm^2. Exposure time: 100 ms. Scale bar: 1 mm. Adapted from ref. [12]. Copyright (2018) The Electrochemical Society

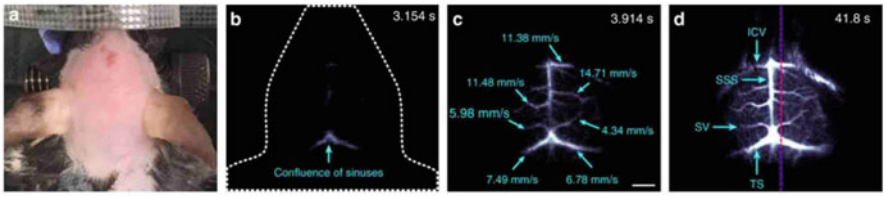

Fig. 13.13 Fast in vivo brain imaging with Er-doped nanoprobes in the 2nd NIR region. (**a**) Color photograph of a C57Bl/6 mouse preceding NIR fluorescence imaging. (**b**–**d**) Time-course NIR brain fluorescence images (exposure time: 20 ms) showing the perfusion of Er-doped nanoprobes into various cerebral vessels. Reproduced from ref. [104] with permission from Springer-Nature

is lower than that of nanomaterial-based NIR nanoprobes because of the smaller extinction coefficients of organic dyes. To overcome the low fluorescence brightness, several efforts have been made to increase the fluorescence brightness of organic dye-based NIR probes.

Wan et al. reported a bright organic NIR nanoprobe (p-FE) for three-dimensional imaging of cerebral vasculatures [66]. They encapsulated an organic NIR dye (FE) in the hydrophobic interior of an amphiphilic polymer, poly (styrene-co-chloromethyl styrene)-graft-poly(ethylene glycol) (PS-*g*-PEG), to produce a bright and biocompatible NIR nanoprobe (size: 12 nm) that can be used for the fluorescence imaging in the 2nd NIR window. The fluorescence quantum yield of p-FE in aqueous environment was ca. 16.5%. With this bright organic NIR nanoprobe, non-invasive ultrafast in vivo NIR imaging of cerebral blood vessels with a short

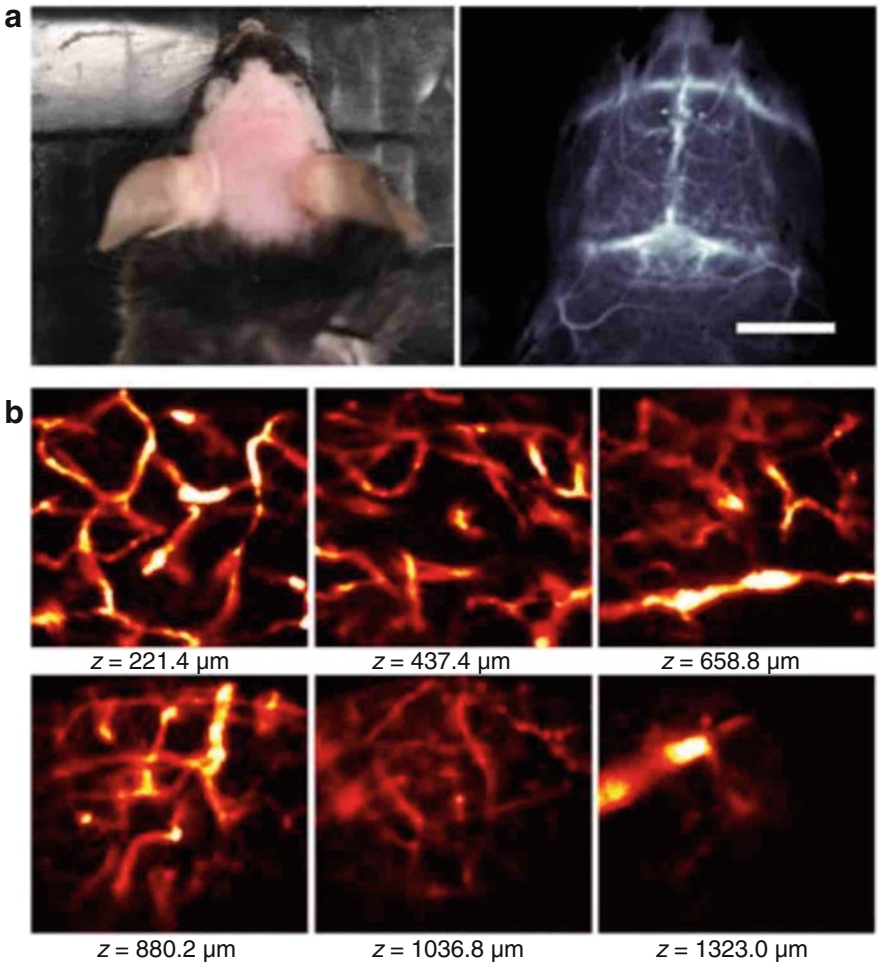

Fig. 13.14 (**a**) Photo and wide-field NIR-II epi-fluorescence imaging of the brain in a mouse injected with p-FE (808 nm excitation, emission >1200 nm) with an exposure time of 5 ms. (**b**) Ex vivo confocal imaging of brain in a mouse injected with p-FE (785 nm excitation, emission >1100 nm, laser power ~30 mW, PMT voltage ~500 V). Reproduced from ref. [66] with permission from Springer-Nature

exposure time of 2–5 ms was achieved (Fig. 13.14). In addition, the bright organic NIR nanoprobe enabled three-dimensional NIR fluorescence imaging of cerebral blood vessels using a confocal imaging system.

13.5.2 Brain Tumors

NIR fluorescence imaging is useful for the non-invasive visualization of brain tumors as well as cerebral blood vessels in living mice. In 2016, Antaris et al. reported a small NIR dye (CH1055) for mouse brain imaging in the 2nd NIR window [65]. They synthesized a small molecule (CH1055, 0.97 kDa) and PEGylated CH1055 (8.9 kDa) and showed the capability of these NIR organic nanoprobes for orthotopic glioblastoma brain tumor imaging. They used an orthotopic glioblastoma brain tumor-bearing mouse by implanting U87MG cells in the mouse brain at a depth of 4 mm with the left hemisphere (Fig. 13.15a, b). Once the brain tumor reached a diameter of 2–3 mm, they intravenously injected PEGylated CH1055 (100 μg) to the mouse and observed NIR fluorescence from the tumor at periodic time points over next 3 days. They observed that 6 h post-injection, the tumor was clearly visible during high magnification of NIR fluorescence (>1200 nm) imaging (Fig. 13.15c). After 24 h, the tumor was clearly visible with a tumor-to-normal tissue ration of 4.25 when using a whole-body imaging system (Fig. 13.15d). In

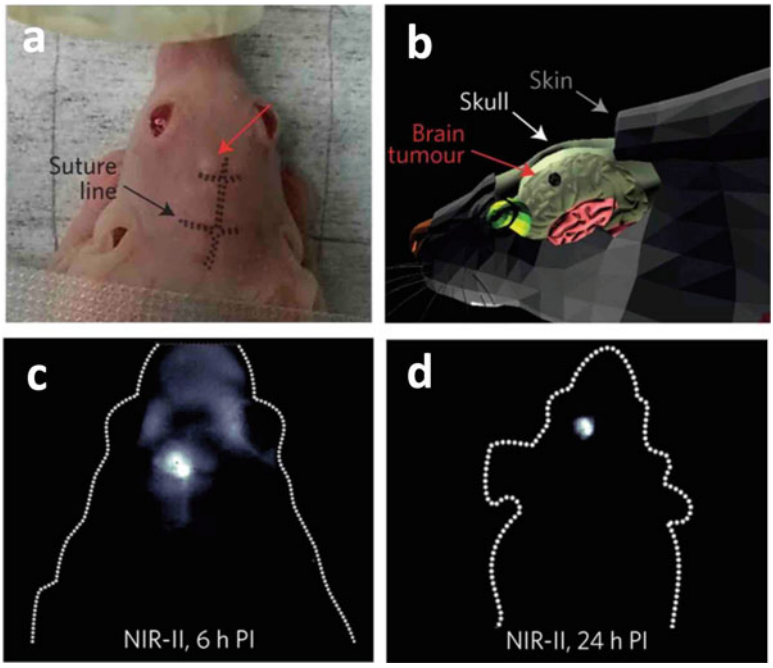

Fig. 13.15 (**a**) Color photograph of a nude mouse preceding high-magnification NIR-II imaging, with an outline over suture lines. (**b**) Graphic representation demonstrating the location of a U87MG orthotopic glioblastoma brain tumor under both the scalp and skull. (**c**, **d**) High-magnification NIR-II fluorescence imaging (1200 nm long-pass filter, 800 ms) showing strong tumor fluorescence detectable through both the scalp and skull 6 h post-intravenous injection. Reproduced from ref. [65] with permission from Springer-Nature

this study, the accumulation of PEGylated CH1055 to a brain tumor was attributed to passive tumor uptake via the enhanced permeation and enhanced (EPR) effect [108]. Recently, Tian et al. reported the fluorescence imaging of a glioblastoma brain tumor by using active tumor uptake of RGD peptide-conjugated NIR dye (IR-BEMC6P@RGD) [76]. They detected strong tumor fluorescence (>1300 nm) through scalp/skull at 12 h post-injection.

13.5.3 Cerebrovascular Disorders

NIR fluorescence imaging can be also used for the visualization of the pathophysiological state of blood vessels in sepsis. Thrombosis in cerebral blood vessels is induced by administration of lipopolysaccharide (LPS) to mice (Fig. 13.16a). Heparin is used as an inhibitor of blood coagulation [109–111]. The magnified images with the scalp removed (Fig. 13.16b) of blood vessels, showed septic clots (i.e., thrombosis), and the number of clots was increased by administration of LPS. The administration of heparin resulted in the suppression of the number of clots (Fig. 13.16b and c). Figure 13.16d shows the immunohistochemistry for an LPS-administrated brain slice, indicating the formation of clots in cerebral blood vessels. The blood coagulation was quantified by enzyme-linked immunosorbent assays (ELISA) (Fig. 13.16e). Thrombin–antithrombin complex (TAT) is a valid biomarker for disseminated intravascular coagulation [112]. After administration of LPS, averaged TAT values were significantly increased, and the level of TAT was recovered by heparin administration. This study suggests that 2nd NIR fluorescence imaging is useful for the detection of thrombosis in an LPS-injected mouse.

13.6 Summary and Outlook

In this chapter, we presented recent progress in NIR fluorescent nanoprobes and techniques for brain imaging in the 2nd NIR window. During the past 5 years, a variety of the NIR nanoprobes have been synthesized, and the proof of principle studies on their capabilities for non-invasive brain imaging have been performed. The pioneer work by Dai group using SWNTs has proven the advantages of NIR fluorescence imaging of brain tissues in the 2nd NIR window [31]: deeper penetration, reduced scattering, and low-autofluorescence in deep-tissue imaging. Nanomaterial-based NIR nanoprobes such as Ag_2S QDs, PbS QDs, and rare earth-doped nanoparticles have also contributed to prove their superior properties for brain imaging. Although the nanomaterial-based NIR nanoprobes such as SWNTs cannot be applied to clinical fields because of their cytotoxic properties, these NIR nanoprobes should be very useful for the study of cancer cell metastasis, immune/inflammatory response, and stem cell dynamics in the animal level.

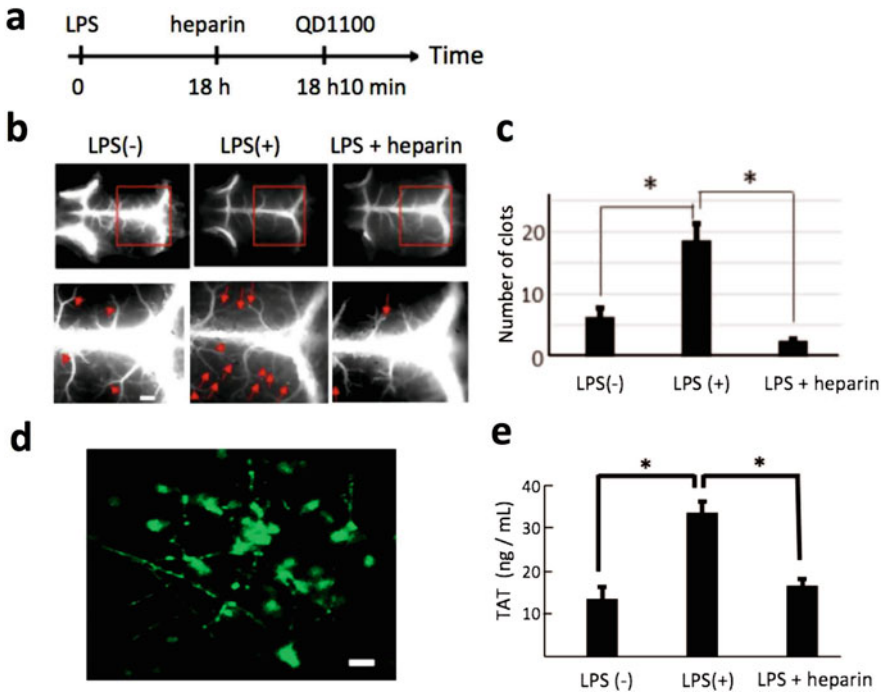

Fig. 13.16 (**a**) Time course of the experimental procedure for LPS and heparin administration. (**b**) NIR fluorescence images (>1000 nm) of cerebral blood vessels before and after administration of LPS (LPS (−) and LPS (+)) and the image followed by additional administration of heparin (LPS + heparin), with scalp removed. Lower panel shows the magnification of the images shown by red rectangular. Red arrowheads show clots. Scale bars: 1 mm. (**c**) Statistical analyses of the clots in the cerebral vessels. (**d**) Immunofluorescence staining of LPS-treated cerebral blood vessels, where anti-fibrinogen antibody (Alexa FLuor 488) was used for staining of fibrinogen. Fibrinogen helps the formation of blood clots. Scale bar: 10 μm. (**e**) ELISA assays for TAT in blood plasma. Adapted from ref. [41]

For biomedical and clinical applications in humans, the NIR nanoprobes must be rapidly metabolized and excluded from the body. The renal filtration threshold for rapid clearance via urine excretion is known as ca. 5 nm [113]. In this regard, smaller organic dye nanoprobes are suitable as NIR probes for fluorescence imaging in humans. In a few years, researchers have developed several types of NIR-dye nanoprobes that emit over 1000 nm [62–91]. These organic NIR nanoprobes have shown the possible application of NIR intravital imaging to biomedical fields. Notably, recent studies showed that the FDA-approved NIR dye, ICG can be used to perform in vivo NIR imaging over 1000 nm. This finding permits the rapid translocation of 2nd NIR-emitting organic dyes (>1000 nm) in the clinical fields.

In the practical use of the 2nd NIR-emitting organic dyes in the clinical fields, high brightness and safety are necessary as optical contrast agents. At the same time, highly sensitive NIR imaging system with a high spatiotemporal resolution should

also be developed for the clinical use such as non-invasive visualization of blood vessels and tumors. At present, except for conventional NIR imaging system (700–900 nm for animals, there is no NIR fluorescence (>1000 nm) imaging system for humans [114]. In the near future, by developing highly sensitive 2nd NIR-emitting organic dyes and intravital imaging system, NIR fluorescence imaging in the 2nd NIR window will be an indispensable tool for non-invasive imaging in biomedical and clinical fields [115].

Acknowledgements The authors thank Setsuko Tsuboi, Sayuri Yamada and Satoko Masa for their help with manuscript preparation.

References

1. Liu H, Beauvoit B, Kimura M, Chance BJ (1996) Dependence of tissue optical properties on solute-induced changes in refractive index and osmolarity. J Biomed Opt 1:200–211
2. Lim YT, Kim S, Nakayama A, Stott NE, Bawendi MG, Frangioni JV (2003) Selection of quantum dot wavelengths for biomedical assays and imaging. Mol Imaging 2:50–64
3. Terai T, Nagano T (2008) Fluorescent probes for bioimaging applications. Curr Opin Chem Biol 12:515–521
4. Joo C, Balci H, Ishitsuka Y, Buranachai C, Ha T (2008) Advances in single-molecule fluorescence methods for molecular biology. Annu Rev Biochem 77:51–76
5. Weissleder R (2001) A clearer vision for *in vivo* imaging. Nat Biotechnol 19:316–317
6. Zhang RR, Schroeder AB, Grudzinski JJ, Rosenthal EL, Warram JM, Pinchuk AN, Eliceiri KW, Kuo JS, Weichert JP (2017) Beyond the margins: real-time detection of cancer using targeted fluorophores nanoprobes. Nat Rev Clin Oncol 14:347–364
7. Namikawa T, Sato T, Hanazaki K (2015) Recent advances in near-infrared fluorescence-guided imaging surgery using indocyanine green. Surg Today 45:1467–1474
8. Liu Z, Yang K, Lee ST (2011) Single-walled carbon nanotubes in biomedical imaging. J Mater Chem 21:586–598
9. Aswathy RG, Yoshida Y, Maekawa T, Kumar DS (2010) Near-infrared quantum dots for deep tissue imaging. Anal Bioanal Chem 397:1417–1435
10. Smith AM, Mancini MC, Nie S (2009) second window for *in vivo* imaging. Nat Nanotechnol 4:710–711
11. Shi L, Sordillo LA, Rodriguez-Contreras A, Alfano R (2016) Transmission in near-infrared optical windows for deep brain imaging. J Biophotonics 9:38–43
12. Tsuboi S, Yamada S, Nakane Y, Sakata T, Yasuda H, Jin T (2018) Water-soluble near-infrared fluorophores emitting over 1000 nm and their application to in vivo imaging in the second optical window (1000-1400 nm). ECS J Solid State Sci Technol 7:R3093–R3101
13. Shi L, Alfano R (eds) (2017) Deep imaging in tissue and biomedical materials. Pan Stanford Publishing, Singapore
14. Hemmer E, Acosta-Mora P, Mendez-Ramos J, Fischer S (2017) Optical nanoprobes for biomedical applications: shining a light on upconverting and near-infrared emitting nanoparticles for imaging, thermal sensing, and photodynamic therapy. J Mater Chem B 5:4365–4392
15. Pan J, Li F, Choi JH (2017) Single-walled carbon nanotubes as optical probes for bio-sensing and imaging. J Mater Chem B 5:6511–6522
16. Cherukuri P, Bachilo SM, Litovsky SH, Weisman RB (2004) Near-infrared fluorescence microscopy of single-walled carbon nanotubes in phagocytic cells. J Am Chem Soc 126:15638–15639

17. Lefebvre J, Austing DG, Bond J, Finnie P (2006) Photoluminescence imaging of suspended single-walled carbon nanotubes. Nano Lett 6:1603–1608
18. Crochet J, Clemens M, Hertel T (2007) Quantum yield heterogeneities of aqueous single-wall carbon nanotube suspensions. J Am Chem Soc 129:8058–8059
19. Leeuw TK, Reith RM, Simonette RA, Harden ME, Cherukuri P, Tsyboulski DA, Beckingham KM, Weisman RB (2007) Single-walled carbon nanotubes in the intact organism: near-ir imaging and biocompatibility studies in drosophila. Nano Lett 7:2650–2654
20. Liu Z, Cai W, He L, Nakayama N, Chen K, Sun X, Chen X, Dai H (2007) *In vivo* biodistribution and highly efficient tumour targeting of carbon nanotubes in mice. Nat Nanotechnol 2:47–52
21. Jin H, Heller DA, Strano MS (2008) Single-particle tracking of endocytosis and exocytosis of single-walled carbon nanotubes in NIH-3T3 cells. Nano Lett 8:1577–1585
22. Welsher K, Liu Z, Daranciang D, Dai H (2008) Selective probing and imaging of cells with single walled carbon nanotubes as near-infrared fluorescent molecules. Nano Lett 8:586–590
23. Jin H, Heller DA, Sharma R, Strano MS (2009) Size-dependent cellular uptake and expulsion of single-walled carbon nanotubes: single particle tracking and a generic uptake model for nanoparticles. ACS Nano 3:149–158
24. Welsher K, Liu Z, Sherlock SP, Robinson JT, Chen Z, Daranciang D, Dai H (2009) A route to brightly fluorescent carbon nanotubes for near-infrared imaging in mice. Nat Nanotechnol 4:773–780
25. Welsher K, Sherlock SP, Dai H (2011) Deep-tissue anatomical imaging of mice using carbon nanotube fluorophores in the second near-infrared window. Proc Natl Acad Sci U S A 108:8943–8948
26. Hong G, Lee JC, Robinson JT, Raaz U, Xie L, Huang NF, Cooke JP, Dai H (2012) Multifunctional *in vivo* vascular imaging using near-infrared II fluorescence. Nat Med 18:1841–1846
27. Yi H, Ghosh D, Ham MH, Qi J, Barone PW, Strano MS, Belcher AM (2012) M13 phage-functionalized single-walled carbon nanotubes as nanoprobes for second near-infrared window fluorescence imaging of targeted tumors. Nano Lett 12:1176–1183
28. Robinson JT, Hong G, Liang Y, Zhang B, Yaghi OK, Dai H (2012) *In vivo* fluorescence imaging in the NIR-II with long circulating carbon nanotubes capable of ultra-high tumor uptake. J Am Chem Soc 134:10664–10669
29. Diao S, Hong G, Robinson JT, Jiao L, Antaris AL, Wu JZ, Choi CL, Dai H (2012) Chirality enriched (12,1) and (11,3) single-walled carbon nanotubes for biological imaging. J Am Chem Soc 134:16971–16974
30. Ghosh D, Bagley AF, Na YJ, Birrer MJ, Bhatia SN, Belcher AM (2014) Deep, noninvasive imaging and surgical guidance of submillimeter tumors using targeted M13-stabilized single-walled carbon nanotubes. Proc Natl Acad Sci U S A 111:13948–13953
31. Hong G, Diao S, Chang J, Antaris AL, Chen C, Zhang B, Zhao S, Atochin DN, Huang PL, Andreasson KI, Kuo CJ, Dai H (2014) Through-skull fluorescence imaging of the brain in a new near-infrared window. Nat Photon 8:723–730
32. Bisesi JH, Ngo T, Ponnavolu S, Liu K, Lavelle CM, Afrooz AR, Saleh NB, Ferguson PL, Denslow ND, Sabo-Attwood T (2015) Examination of single-walled carbon nanotubes uptake and toxicity from dietary exposure: tracking movement and impacts in the gastrointestinal system. Nanomaterials 5:1066–1086
33. Nakane Y, Tsukasaki Y, Sakata T, Yasuda H, Jin T (2013) Aqueous synthesis of glutathione-coated PbS quantum dots with tunable emission for non-invasive fluorescence imaging in the second near-infrared biological window (1000–1400 nm). Chem Commun 49:7584–7586
34. Tsukasaki Y, Morimatsu M, Nishimura G, Sakata T, Yasuda H, Komatsuzaki A, Watanabe TM, Jin T (2014) Synthesis and optical properties of emission-tunable PbS/CdS core–shell quantum dots for *in vivo* fluorescence imaging in the second near-infrared window. RSC Adv 4:41164–41171

35. Tsukasaki Y, Komatsuzaki A, Mori Y, Ma Q, Yoshioka Y, Jin T (2014) A short-wavelength infrared emitting multimodal probe for non-invasive visualization of phagocyte cell migration in living mice. Chem Commun 50:14356–14359
36. Corricelli M, Depalo N, Carlo ED, Fanizza E, Laquintana V, Denora N, Agostiano A, Striccoli M, Curri ML (2014) Biotin-decorated silica coated PbS nanocrystals emitting in the second biological near infrared window for bioimaging. Nanoscale 6:7924–7933
37. Sasaki A, Tsukasaki Y, Komatsuzaki A, Sakata T, Yasuda H, Jin T (2015) Recombinant protein (EGFP-protein G)-coated PbS quantum dots for *in vitro* and *in vivo* dual fluorescence (visible and second-NIR) imaging of breast tumors. Nanoscale 7:5115–5119
38. Benayas A, Ren F, Carrasco E, Marzal V, del Rosal B, Gonfa BA, Juarranz A, Sanz-Rodriguez F, Jaque D, Garcia-Sole J, Ma D, Vetrone F (2015) PbS/CdS/ZnS quantum dots: a multifunctional platform for in vivo near-infrared low-dose fluorescence imaging. Adv Funct Mater 25:6650–6659
39. Wu K, Zhang J, Fan S, Li J, Zhang C, Qiao K, Qian L, Han J, Tang J, Wang S (2015) Plasmon-enhanced fluorescence of PbS quantum dots for remote near-infrared imaging. Chem Commun 51:141–144
40. Jin T, Imamura Y (2016) Applications of highly bright PbS quantum dots to non-invasive near-infrared fluorescence imaging in the second optical window. ECS J Solid State Sci Technol 5:R3138–R3145
41. Imamura Y, Yamada S, Tsuboi S, Nakane Y, Tsukasaki Y, Komatsuzaki A, Jin T (2016) Near-infrared emitting PbS quantum dots for *in vivo* fluorescence imaging of the thrombotic state in septic mouse brain. Molecules 21:1080
42. Chen J, Kong Y, Wang W, Fang H, Wo Y, Zhou D, Wu Z, Li Y, Chen S (2016) Direct water-phase synthesis of lead sulfide quantum dots encapsulated by β-lactoglobulin for *in vivo* second near infrared window imaging with reduced toxicity. Chem Commun 52:4025–4028
43. Kong Y, Chen J, Fang H, Heath G, Wo Y, Wang W, Li Y, Guo Y, Evans SD, Chen S, Zhou D (2016) Highly fluorescent ribonuclease-A-encapsulated lead sulfide quantum dots for ultrasensitive fluorescence *in vivo* imaging in the second near-infrared window. Chem Mater 28:3041–3050
44. Du Y, Xu B, Fu T, Cai M, Li F, Zhang Y, Wang Q (2010) Near-infrared photoluminescent Ag_2S quantum dots from a single source precursor. J Am Chem Soc 132:1470–1471
45. Hong G, Robinson JT, Zhang Y, Diao S, Antaris AL, Wang Q, Dai H (2012) *In vivo* fluorescence imaging with Ag_2S quantum dots in the second near-infrared region. Angew Chem Int Ed 51:9818–9821
46. Jiang P, Tian ZQ, Zhu CN, Zhang ZL, Pang DW (2012) Emission-tunable near-infrared Ag_2S quantum dots. Chem Mater 24:3–5
47. Zhang Y, Hong G, Zhang Y, Chen G, Li F, Dai H, Wang Q (2012) Ag_2S quantum dot: a bright and biocompatible fluorescent nanoprobe in the second near-infrared window. ACS Nano 6:3695–3702
48. Jiang P, Zhu CN, Zhang ZL, Tian ZQ, Pang DW (2012) Water-soluble Ag_2S quantum dots for near-infrared fluorescence imaging *in vivo*. Biomaterials 33:5130–5135
49. Yang HY, Zhao YW, Zhang ZY, Xiong HM, Yu SN (2013) One-pot synthesis of water-dispersible Ag_2S quantum dots with bright fluorescent emission in the second near-infrared window. Nanotechnology 24:055706
50. Zhang Y, Zhang Y, Hong G, He W, Zhou K, Yang K, Li F, Chen G, Liu Z, Dai H, Wang Q (2013) Biodistribution, pharmacokinetics and toxicology of Ag_2S near-infrared quantum dots in mice. Biomaterials 34:3639–3646
51. Zhang Y, Liu Y, Li C, Chen X, Wang Q (2014) Controlled synthesis of Ag_2S quantum dots and experimental determination of the exciton bohr radius. J Phys Chem C 118:4918–4923
52. Gui R, Wan A, Liu X, Yuan W, Jin H (2014) Water-soluble multidentate polymers compactly coating Ag_2S quantum dots with minimized hydrodynamic size and bright emission tunable from red to second near-infrared region. Nanoscale 6:5467–5473

53. Li C, Zhang Y, Wang M, Zhang Y, Chen G, Li L, Wu D, Wang Q (2014) *In vivo* real-time visualization of tissue blood flow and angiogenesis using Ag_2S quantum dots in the NIR-II window. Biomaterials 35:393–400
54. Chen G, Tian F, Li C, Zhang Y, Weng Z, Zhang Y, Peng R, Wang Q (2015) *In vivo* real-time visualization of mesenchymal stem cells tropism for cutaneous regeneration using NIR-II fluorescence imaging. Biomaterials 53:265–273
55. Li C, Li F, Zhang Y, Zhang W, Zhang XE, Wang Q (2015) Real-time monitoring surface chemistry-dependent *in vivo* behaviors of protein nanocages via encapsulating an NIR-II Ag_2S quantum dot. ACS Nano 9:12255–12263
56. Chen J, Kong Y, Wo Y, Fang H, Li Y, Zhang T, Dong Y, Ge Y, Wu Z, Zhou D, Chen S (2016) Facile synthesis of β-lactoglobulin capped Ag_2S quantum dots for *in vivo* imaging in the second near-infrared biological window. J Mater Chem B 4:6271–6278
57. Wu Q, Zhou M, Shi J, Li Q, Yang M, Zhang Z (2017) Synthesis of water-soluble Ag_2S quantum dots with fluorescence in the second near-infrared window for turn-on detection of Zn(II) and Cd(II). Anal Chem 89:6616–6623
58. Kamimura M, Kanayama N, Tokuzen K, Soga K, Nagasaki Y (2011) Near-infrared (1550 nm) *in vivo* bioimaging based on rare-earth doped ceramic nanophosphors modified with PEG-b-poly(4-vinylbenzylphosphonate). Nanoscale 3:3705–3713
59. Naczynski DJ, Tan MC, Zevon M, Wall B, Kohl J, Kulesa A, Chen S, Roth CM, Riman RE, Moghe PV (2013) Rare-earth-doped biological composites as *in vivo* shortwave infrared reporters. Nat Commun 4:2199
60. Zevon M, Ganapathy V, Kantamneni H, Mingozzi M, Kim P, Adler D, Sheng Y, Tan MC, Pierce M, Riman RE, Roth CM, Moghe PV (2015) CXCR-4 targeted, short wave infrared (SWIR) emitting nanoprobes for enhanced deep tissue imaging and micrometastatic cancer lesion detection. Small 11:6347–6357
61. Shao W, Chen G, Kuzmin A, Kutscher HL, Pliss A, Ohulchanskyy TY, Prasad PN (2016) Tunable narrow band emissions from dye-sensitized core/shell/shell nanocrystals in the second near-infrared biological window. J Am Chem Soc 138:16192–16195
62. Tao Z, Hong G, Shinji C, Chen C, Diao S, Antaris AL, Zhang B, Zou Y, Dai H (2013) Biological imaging using nanoparticles of small organic molecules with fluorescence emission at wavelengths longer than 1000 nm. Angew Chem Int Ed 52:13002–13006
63. Hong G, Zou Y, Antaris AL, Diao S, Wu D, Cheng K, Zhang X, Chen C, Liu B, He Y, Wu JZ, Yuan J, Zhang B, Tao Z, Fukunaga C, Dai H (2014) Ultrafast fluorescence imaging in vivo with conjugated polymer fluorophores in the second near-infrared window. Nat Commun 5:4206
64. Antaris AL, Chen H, Diao S, Ma Z, Zhang Z, Zhu S, Wang J, Lozano AX, Fan Q, Chew L, Zhu M, Cheng K, Hong X, Dai H, Cheng Z (2017) A high quantum yield molecule-protein complex fluorophore for near-infrared II imaging. Nat Commun 8:15269
65. Antaris AL, Chen H, Cheng K, Sun Y, Hong G, Qu C, Diao S, Deng Z, Hu X, Zhang B, Zhang X, Yaghi OK, Alamparambil ZR, Hong X, Cheng Z, Dai H (2016) A small-molecule dye for NIR-II imaging. Nat Mater 15:235–242
66. Wan H, Yue J, Zhu S, Uno T, Zhang X, Yang Q, Yu K, Hong G, Wang J, Li L, Ma Z, Gao H, Zhong Y, Su J, Antaris AL, Xia Y, Luo J, Liang Y, Dai H (2018) A bright organic NIR-II nano fluorophore for three-dimensional imaging into biological tissues. Nat Commun 9:1171
67. Li B, Lu L, Zhao M, Lei Z, Zhang F (2018) An efficient 1064 nm NIR-II excitation fluorescent molecular dye for deep-tissue high-resolution dynamic bioimaging. Angew Chem Int Ed 57:7483–7487
68. Zhang XD, Wang H, Antaris AL, Li L, Diao S, Ma R, Nguyen A, Hong G, Ma Z, Wang J, Zhu S, Castellano JM, Wyss-Coray T, Liang Y, Luo J, Dai H (2016) Traumatic brain injury imaging in the second near-infrared window with a molecular fluorophore. Adv Mater 28:6872–6879
69. Shou K, Qu C, Sun Y, Chen H, Chen S, Zhang L, Xu H, Hong X, Yu A, Cheng Z (2017) Multifunctional biomedical imaging in physiological and pathological conditions using a NIR-II probe. Adv Funct Mater 27:1700995

70. Guo B, Sheng Z, Kenry Hu D, Lin X, Xu S, Liu C, Zheng H, Liu B (2017) Biocompatible conjugated polymer nanoparticles for highly efficient photoacoustic imaging of orthotopic brain tumors in the second near-infrared window. Mater Horiz 4:1151–1156
71. Jiang Y, Upputuri PK, Xie C, Lyu Y, Zhang L, Xiong Q, Paramanik M, Pu K (2017) Broadband absorbing semiconducting polymer nanoparticles for photoacoustic imaging in second near-infrared window. Nano Lett 17:4964–4969
72. Bhavane R, Starosolski Z, Stupin I, Ghaghada KB, Annapragada A (2018) NIR-II fluorescence imaging using indocyanine green nanoparticles. Sci Rep 8:14455
73. Carr JA, Franke D, Caram JR, Perkinson CF, Saif M, Askoxylakis V, Datta M, Fukumura D, Jain RK, Bawendi MG, Bruns OT (2018) Shortwave infrared fluorescence imaging with the clinically approved near-infrared dye indocyanine green. Proc Natl Acad Sci U S A 115:4465–4470
74. Kurbegovic S, Juhl K, Chen H, Qu C, Ding B, Leth JM, Drzewiecki KT, Kjaer A, Cheng Z (2018) Molecular targeted NIR-II probe for image-guided brain tumor surgery. Bioconjug Chem 29:3833–3840
75. Qi J, Sun C, Li D, Zhang H, Yu W, Zebibula A, Lam JWY, Xi W, Zhu L, Cai F, Wei P, Zhu C, Kwok RTK, Streich LL, Prevedel R, Qian J, Tang BZ (2018) Aggregation-induced emission luminogen with near-infrared-II excitation and near-infrared-I emission for ultradeep intravital two-photon microscopy. ACS Nano 12:7936–7945
76. Tian R, Ma H, Yang Q, Wan H, Zhu S, Chandra S, Sun H, Kiesewetter DO, Niu G, Liang Y, Chen X (2019) Rational design of a super-contrast NIR-II fluorophore affords high-performance NIR-II molecular imaging guided microsurgery. Chem Sci 10:326–332
77. Ding F, Li C, Xu Y, Li J, Li H, Yang G, Sun Y (2018) PEGylation regulates self-assembled small-molecule dye-based probes from single molecule to nanoparticle size for multifunctional NIR-II bioimaging. Adv Healthc Mater 7:e1800973
78. Sun Y, Qu C, Chen H, He M, Tang C, Shou K, Hong S, Yang M, Jiang Y, Ding B, Xiao Y, Xing L, Hong X, Cheng Z (2016) Novel benzo-bis(1,2,5-thiadiazole) fluorophores for *in vivo* NIR-II imaging of cancer. Chem Sci 7:6203–6207
79. Cosco ED, Caram JR, Bruns OT, Franke D, Day RA, Farr EP, Bawendi MG, Sletten EM (2017) Flavylium polymethine fluorophores for near- and shortwave infrared imaging. Angew Chem Int Ed 56:13126–13129
80. Sun Y, Ding M, Zeng X, Xiao Y, Wu H, Zhou H, Ding B, Qu C, Hou W, Er-Bu A, Zhang Y, Cheng Z, Hong X (2017) Novel bright-emission small-molecule NIR-II fluorophores for *in vivo* tumor imaging and image-guided surgery. Chem Sci 8:3489–3493
81. Zhu S, Yang Q, Antaris AL, Yue J, Ma Z, Wang H, Huang W, Wan H, Wang J, Diao S, Zhang B, Li X, Zhong Y, Yu K, Hong G, Luo J, Liang Y, Dai H (2017) Molecular imaging of biological systems with a clickable dye in the broad 800- to 1,700-nm near-infrared window. Proc Natl Acad Sci U S A 114:962–967
82. Feng Y, Zhu S, Antaris AL, Chen H, Xiao Y, Lu X, Jiang L, Diao S, Yu K, Wang Y, Herraiz S, Yue J, Hong X, Hong G, Cheng Z, Dai H, Hsueh AJ (2017) Live imaging of follicle stimulating hormone receptors in gonads and bones using near infrared II fluorophore. Chem Sci 8:3703–3711
83. Starosolski Z, Bhavane R, Ghaghada KB, Vasudevan SA, Kaay A, Annapragada A (2017) Indocyanine green fluorescence in second near-infrared (NIR-II) window. PLoS One 12:e0187563
84. Sun Y, Zeng X, Xiao Y, Liu C, Zhu H, Zhou H, Chen Z, Xu F, Wang J, Zhu M, Wu J, Tian M, Zhang H, Deng Z, Cheng Z, Hong X (2018) Novel dual-function near-infrared II fluorescence and PET probe for tumor delineation and image-guided surgery. Chem Sci 9:2092–2097
85. Zhu S, Hu Z, Tian R, Yung BC, Yang Q, Zhao S, Kiesewetter DO, Niu G, Sun H, Antaris AL, Chen X (2018) Repurposing cyanine NIR-I dyes accelerates clinical translation of near-infrared-II (NIR-II) bioimaging. Adv Mater 30:1802546
86. Lin J, Zeng X, Xiao Y, Tang L, Nong J, Liu Y, Zhou H, Ding B, Xu F, Tong H, Deng Z, Hong X (2019) Novel near-infrared II aggregation-induced emission dots for *in vivo* bioimaging. Chem Sci. 10:1219–1226

87. Sheng Z, Guo B, Hu D, Xu S, Wu W, Liew WH, Yao K, Jiang J, Liu C, Zheng H, Liu B (2018) Bright aggregation-induced-emission dots for targeted synergetic NIR-II fluorescence and NIR-I photoacoustic imaging of orthotopic brain tumors. Adv Mater 30:1800766
88. Tang Y, Li Y, Hu X, Zhao H, Ji Y, Chen L, Hu W, Zhang W, Li X, Lu X, Huang W, Fan Q (2018) "Dual lock-and-key"-controlled nanoprobes for ultrahigh specific fluorescence imaging in the second near-infrared window. Adv Mater 30:1801140
89. Shou K, Tang Y, Chen H, Chen S, Zhang L, Zhang A, Fan Q, Yu A, Cheng Z (2018) Diketopyrrolopyrrole-based semiconducting polymer nanoparticles for *in vivo* second near-infrared window imaging and image-guided tumor surgery. Chem Sci 9:3105–3110
90. Lu X, Yuan P, Zhang W, Wu Q, Wang X, Zhao M, Sun P, Huang W, Fan Q (2018) A highly water-soluble triblock conjugated polymer for *in vivo* NIR-II imaging and photothermal therapy of cancer. Polym Chem 9:3118–3126
91. Zhu S, Herraiz S, Yue J, Zhang M, Wan H, Yang Q, Ma Z, Wang Y, He J, Antaris AL, Zhong Y, Diao S, Feng Y, Zhou Y, Yu K, Hong G, Liang Y, Hsueh AJ, Dai H (2018) 3D NIR-II molecular imaging distinguishes targeted organs with high-performance NIR-II bioconjugates. Adv Mater 30:1705799
92. Georgakoudi I, Jacobson BC, Müller MG, Sheets EE, Badizadegan K, Carr-Locke DL, Crum CP, Boone CW, Dasari RR, Van Dam J, Feld MS (2002) NAD(P)H and collagen as in vivo quantitative fluorescent biomarkers of epithelial precancerous changes. Cancer Res 62:682–687
93. Zipfel WR, Williams RM, Christie R, Nikitin AY, Hyman BT, Webb WW (2003) Live tissue intrinsic emission microscopy using multiphoton-excited native fluorescence and second harmonic generation. Proc Natl Acad Sci U S A 100:7075–7080
94. Gallas JM, Eisner M (1987) Fluorescence of melanin-dependence upon excitation wavelength and concentration. Photochem Photobiol 45:595–600
95. Ema M, Gamo M, Honda K (2016) A review of toxicity studies of single-walled carbon nanotubes in laboratory animals. Regul Toxicol Pharmacol 74:42–63
96. Park EJ, Roh J, Kim SN, Kang MS, Lee BS, Kim Y, Choi S (2011) Biological toxicity and inflammatory response of semi-single-walled carbon nanotubes. PLoS One 6:e25892
97. Jin T, Tsuboi S, Komatsuzaki A, Imamura Y, Muranaka Y, Sakata T, Yasuda H (2016) Enhancement of aqueous stability and fluorescence brightness of indocyanine green using small calix[4]arene micelles for near-infrared fluorescence imaging. Med Chem Commun 7:623–631
98. Diao S, Blackburn JL, Hong G, Antaris AL, Chang J, Wu JZ, Zhang B, Cheng K, Kuo CJ, Dai H (2015) Fluorescence imaging in vivo at wavelengths beyond 1500 nm. Angew Chem Int Ed 54:14758–14762
99. Li C, Cao L, Zhang Y, Yi P, Wang M, Tan B, Deng Z, Wu D, Wang Q (2015) Preoperative detection and intraoperative visualization of brain tumors for more precise surgery: a new dual-modality MRI and NIR nanopobe. Small 11:4517–4525
100. Franke D, Harris DK, Chen O, Bruns OT, Carr JA, Wilson MW, Bawendi MG (2016) Continuous injection synthesis of indium arsenide quantum dots emissive in the short-wavelength infrared. Nat Commun 7:12749
101. Bruns OT, Bischof TS, Harris DK, Franke D, Shi Y, Riedemann L, Bartelt A, Jaworski FB, Carr JA, Rowlands CJ, Wilson MWB, Chen O, Wei H, Hwang GW, Montana DM, Coropceanu I, Achorn OB, Kloepper J, Heeren J, So PTC, Fukumura D, Jensen KF, Jain RK, Bawendi MG (2017) Next-generation *in vivo* optical imaging with short-wave infrared quantum dots. Nat Biomed Eng 1:0056
102. Zamberian F, Turyanska L, Patane A, Liu Z, Williams HEL, Fay MW, Clarke PA, Imamura Y, Jin T, Bradshaw TD, Thomas NR, Grabowska AM (2018) Stable DHLA–PEG capped PbS quantum dots: from synthesis to near-infrared biomedical imaging. J Mater Chem B6:550–555
103. Zebibula A, Alifu N, Xia L, Sun C, Yu X, Xue D, Liu L, Li G, Qian J (2018) Ultrastable and biocompatible NIR-II quantum dots for functional bioimaging. Adv Funct Mater 28:1703451

104. Zhong Y, Ma Z, Zhu S, Yue J, Zhang M, Antaris AL, Yuan J, Cui R, Wan H, Zhou Y, Wang W, Huang NF, Luo J, Hu Z, Dai H (2017) Boosting the down-shifting luminescence of rare-earth nanocrystals for biological imaging beyond 1500 nm. Nat Commun 8:737
105. Deng Z, Li X, Xue Z, Jiang M, Li Y, Zeng S, Liu H (2018) A high performance Sc-based nanoprobe for through-skull fluorescence imaging of brain vessels beyond 1500 nm. Nanoscale 10:9393–9400
106. Guo B, Sheng Z, Hu D, Liu C, Zheng H, Liu B (2018) Through scalp and skull NIR-II photothermal therapy of deep orthotopic brain tumors with precise photoacoustic imaging guidance. Adv Mater 30:e1802591
107. Liu W, Wang Y, Han X, Lu P, Zhu L, Sun C, Qian J, He S (2018) Fluorescence resonance energy transfer (FRET) based nanoparticles composed of AIE luminogens and NIR dyes with enhanced three-photon near-infrared emission for *in vivo* brain angiography. Nanoscale 10:10025–10032
108. Kim TH, Mount CW, Dulken BW, Ramos J, Fu CJ, Khant HA, Chiu W, Gombotz WR, Pun SH (2012) Filamentous, mixed micelles of triblock copolymers enhance tumor localization of indocyanine green in a murine xenograft model. Mol Pharm 9:135–143
109. Slofstra SH, van 't Veer C, Buurman WA, Reitsma PH, Ten Cate H, Spek CA (2005) Low molecular weight heparin attenuates multiple organ failure in a murine model of disseminated intravascular coagulation. Crit Care Med 33:1365–1370
110. Ding R, Zhao D, Guo R, Zhang Z, Ma X (2011) Treatment with unfractionated heparin attenuates coagulation and inflammation in endotoxemic mice. Thromb Res 128:e160–e165
111. Li R, Tong J, Tan Y, Zhu S, Yang J, Ji M (2015) Low molecular weight heparin prevents lipopolysaccharide induced-hippocampus-dependent cognitive impairments in mice. Int J Clin Exp Pathol 8:8881–8891
112. Wada H, Wakita Y, Nakase T, Shimura M, Hiyoyama K, Nagaya S, Deguchi H, Mori Y, Kaneko T, Deguchi K, Fujii J, Shiku H (1996) Increased plasma-soluble fibrin monomer levels in patients with disseminated intravascular coagulation. Am J Hematol 51:255–260
113. Choi HS, Liu W, Misra P, Tanaka E, Zimmer JP, Ipe BI, Bawendi MG, Frangioni JV (2007) Renal clearance of quantum dots. Nat Biotechnol 25:1165–1170
114. Li C, Wang Q (2018) Challenges and opportunities for intravital near-infrared fluorescence imaging technology in the second transparency window. ACS Nano 12:9654–9659
115. Schnermann MJ (2017) Chemical biology: organic dyes for deep bioimaging. Nature 551:176–177